Research Article

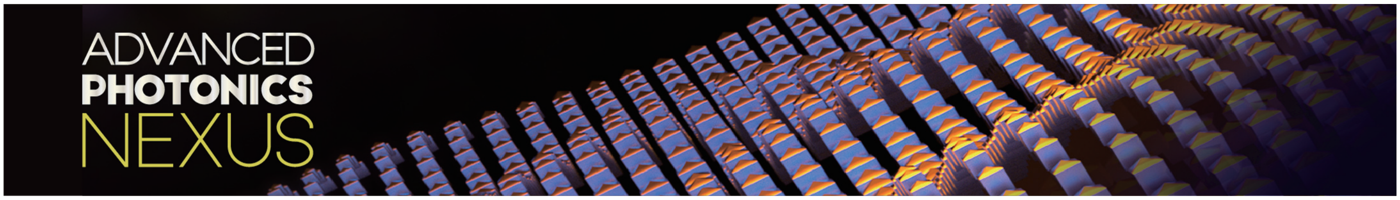

Ultrawide field-of-view integrated optical phased arrays employing multiple orbital angular momentum beams

Zhen Wang,[a] Shuxin Liu,[a] Jingchi Li,[a] Yong Zhang,[a] Xinyuan Fang,[b] Qiwen Zhan,[c] and Yikai Su[a,*]
[a]Shanghai Jiao Tong University, Department of Electronic Engineering and Electrical Engineering, Shanghai, China
[b]University of Shanghai for Science and Technology, School of Artificial Intelligence Science and Technology, Shanghai, China
[c]University of Shanghai for Science and Technology, School of Optical-Electrical and Computer Engineering, Shanghai, China

Abstract. Optical phased arrays (OPAs) are crucial in beam-steering applications, particularly as transmitters in light detection and ranging and free-space communication systems. In this paper, we demonstrate a on-chip OPA that emits multiple orbital angular momentum (OAM) beams in different directions, each carrying unique topological charges. By superimposing a forked 1×3 Dammann grating on the grating array, six OAM beams with topological charges of ± 3, ± 4, and ± 5 can be radiated from the OPA region. The OPA chip was fabricated on a silicon-on-insulator platform, and the simultaneous generation of multiple OAM beams was realized experimentally. The directions of these vortices can be steered by adjusting the wavelength of the input light and the bias voltages of the phase shifters, enabling a remarkable field of view (FOV) of 140 deg × 40 deg within a 120-nm wavelength range. We pave the way for developing systems with ultrawide FOVs, improving the resolution of remote sensing and broadening the possibilities of free-space communications.

Keywords: silicon photonics; optical phased array; orbital angular momentum.

Received Sep. 19, 2024; revised manuscript received Oct. 17, 2024; accepted for publication Nov. 22, 2024; published online Dec. 20, 2024.

[DOI: 10.1117/1.APN.4.1.016005]

1 Introduction

Developed in recent decades, the optical phased array (OPA) technology represents a significant breakthrough in photonics, providing a versatile and dynamic method of manipulating light.[1–9] Similar to the phased arrays utilized in radar, an OPA is an array of closely spaced optical emitters, such as lasers or grating couplers. This technology enables precise control over the phase and amplitude of light waves, achieving the steering, shaping, and focusing of light beams without mechanical movement.[10–13] OPAs find applications in various domains, including communications, light detection and ranging (lidar) systems, medical imaging, and holographic displays.[14–25] Aiming for enhanced surveillance, imaging, and communication capabilities, multibeam OPA schemes have been proposed. Current implementations typically rely on two main approaches: (1) Dammann gratings,[26–28] which divide the input beam into multiple diffraction levels, producing multiple beams, and (2) sparse emitter arrays,[11,29–37] where techniques such as thermal tuning or liquid crystals adjust the phase of individual subarrays, enabling each to emit in a different direction. Compared with the single-beam OPA scheme, multibeam OPA schemes can effectively expand the field of view (FOV), improve the scanning speed, and increase the number of simultaneously handled targets.[28] To reduce the interference among various echoes in multibeam systems, a practical approach is coding the light with orthogonal waveforms, which facilitates the identification of different beams in lidar systems.[38,39] In addition, wavelength and time division multiplexing technologies can help discern the directions of the light beams.[40] However, these approaches require complex digital signal processing (DSP) algorithms to mitigate cross talk among echoes.

Introducing orbital angular momentum (OAM) beams into lidar transmitters can simplify or even eliminate the need for complex DSP in systems, thereby reducing the complexity of electronic chips.[41] OAM beams, characterized by rotating

---

*Address all correspondence to Yikai Su, yikaisu@sjtu.edu.cn wavefronts of $\exp(il\theta)$ (θ is the azimuthal angle and l is the topological charge) and spatial orthogonality among infinite channels,[42–44] introduce a novel dimension of beam control into the OPAs of lidar systems.[45–53] When an obstacle is illuminated by an OAM beam, a spatially varied echo carries more detailed information about the obstacle, providing higher-resolution imaging beyond the Rayleigh limit[54,55] and efficient detection of rotational Doppler shifts.[56] Moreover, as an OAM light beam travels through the atmosphere, its phase and intensity distribution can be affected by atmospheric turbulence. Upon reflection, the echo experiences the same phase and intensity distortions in reverse order, effectively canceling out the atmosphere disturbances imposed on the propagation path of the beam.[57] Thus, as the transmitter in a lidar system, using OAM beams in the OPA can provide a robust and accurate method of enhancing the imaging resolution and maintaining signal integrity despite atmospheric interferences.[58–60] The existing schemes generate multiple indistinguishable Gaussian beams or single OAM beams[43–47,61–64] for ranging or communication purposes. To date, no OPA scheme exists that can simultaneously diffract OAM beams that carry different topological charges for the purpose of beam identification.

To address this issue, we propose an on-chip multi-OAM-beam OPA scheme. The OPA consists of a pair of phase shifter arrays and a forked Dammann grating array, which effectively couple the in-plane guided mode to the out-of-plane OAM beams carrying different topological charges. We fabricated the proposed multibeam OAM OPA chip on a 220-nm-thick commercial silicon-on-insulator (SOI) platform. By injecting light beams from both the left and right sides of the 1×3 Dammann grating, six $(3+3)$ diffracted beams can cover a 140-deg FOV in azimuth within a wavelength range of 120 nm. These beams can also be precisely deflected using thermal phase shifters within ±20 deg in elevation. The experimental results show that the proposed scheme enables an ultralarge FOV of 140 deg ×40 deg, significantly surpassing traditional two-dimensional (2D) beam-steering approaches. Our design serves as a practical integrated OPA for OAM multibeam generation and steering. Compared with other multibeam OPA schemes, this approach enables the identification of multiple beams by simply addressing multiple topological charges. By strategically selecting the diffraction orders and angles, we also achieved the largest FOV documented in this field, to the best of our knowledge.

2 Results

Figure 1(a) shows the designed multiple-OAM OPA chip, which enables 2D multibeam forming and steering. This functionality is achieved by tuning the wavelength of light to steer beams in the θ dimension and by heating phase shifters to rotate beams in the φ dimension. The key feature of the design is the forked 1×3 Dammann grating array, which is superimposed on a binary holographic fork grating. The forked 1×3 Dammann grating array consists of two structures: a 1×3 Dammann grating array and a waveguide–grating directional coupler (WG-DC) array. This configuration is essential for uniformly diffracting in-plane guided-mode light into three distinct OAM beams in free space. In Fig. 1(b), the distribution of the fork Dammann grating array is given by

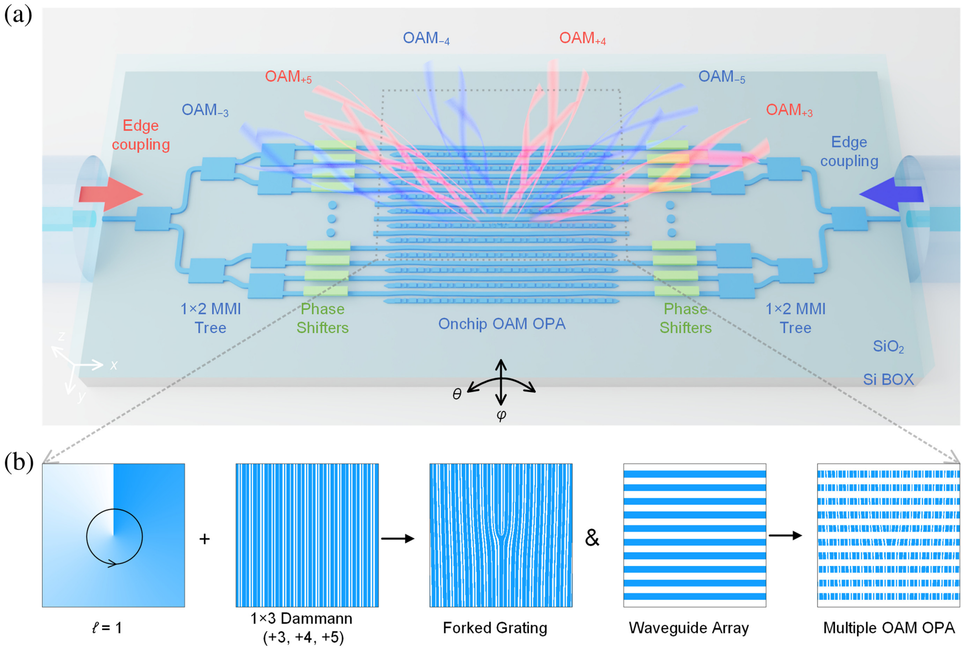

Fig. 1 Working principle of emitting OAM beams with different topological charges using an on-chip OPA. (a) Schematic of the proposed OAM OPA chip, detailing the essential components and interconnection structures. (b) Method of generating the proposed multiple-OAM OPA. The etching pattern of the forked grating is achieved using a spiral phase distribution ($l = 1$) and a 1×3 Dammann grating array. The layout of the multiple-OAM OPA is the intersection of the forked grating and the waveguide array.

$$\phi(r,\varphi) = l\varphi + kr\cos\varphi, \mathrm{Hologram}(\phi) = \begin{cases} 1 & \mathrm{mod}(\phi, 2\pi)\ \Lambda \in L_1, L_3, L_5 \\ 0 & \text{others} \end{cases}, \qquad (1)$$

where l represents the topological charge of the holograph [l is an integer number, and $l = +1$ in Fig. 1(a)], and k is the propagation constant of the silicon waveguide mode. L_1 to L_6 are the optimized structural parameters of the 1×3 Dammann gratings, as shown in Fig. 2(a).

For the m'th-order diffraction, the phase difference among the light diffracted by neighboring cells in a grating is multiplied times m. Therefore, each m'th-order vortex diffracted by the forked Dammann grating array carries a topological charge of ml. As depicted in Fig. 1(a), the forked Dammann grating array design enables the uniform diffraction of bidirectional input lights into six diffraction orders ($m = \pm 3$, ± 4, and ± 5). Consequently, six OAM beams, carrying different topological charges ($ml = \pm 3$, ± 4, and ± 5), effectively sweep six sub-FOVs.

2.1 1 × 3 Dammann Grating

We employed a 1×3 Dammann grating and binary-phase Fourier hologram to generate an array of point sources, thereby simultaneously generating multiple beams. Because on-chip surface-emitting Dammann gratings have not been extensively discussed in the literature, we ran a parameter sweep to obtain the far-field intensities for various grating periods. The etching parameters are determined through subsequent optimization, as detailed in the Supplementary Material. Figure 2(a) shows a three-dimensional (3D) schematic of the optimized 1×3 Dammann grating. We chose a grating width $W = 0.5\ \mu$m and period $\Lambda = 2.6\ \mu$m, which radiates diffraction orders +3 through +5 into free space. The red regions in Fig. 2(b) indicate blind zones, which remain despite the large bandwidth of 160 nm. To address the blind zones, two beams are input from both sides, causing the grating to diffract three OAM pairs of opposite orders, as illustrated in Fig. 2(c). In addition, the low efficiencies of the three diffractions at 1510 nm are attributed to the exact fulfillment of the high-order Bragg condition.

2.2 Waveguide–Grating Directional Coupler

We propose a WG-DC structure [Fig. 2(e)] comprising a 1×3 Dammann grating and a strip waveguide to extend the antenna aperture beyond 100 μm and to improve the mode purity of the OAM beams. Due to the exponential attenuation of power, the practical length of a 70-nm-etched grating is constrained to less than 35 μm. In our design, we place a symmetrically bent waveguide adjacent to a straight grating to establish a DC structure. By precisely manipulating the gap between the grating and waveguide, the power distribution in the grating conforms to a Gaussian distribution. This approach enables the flexible

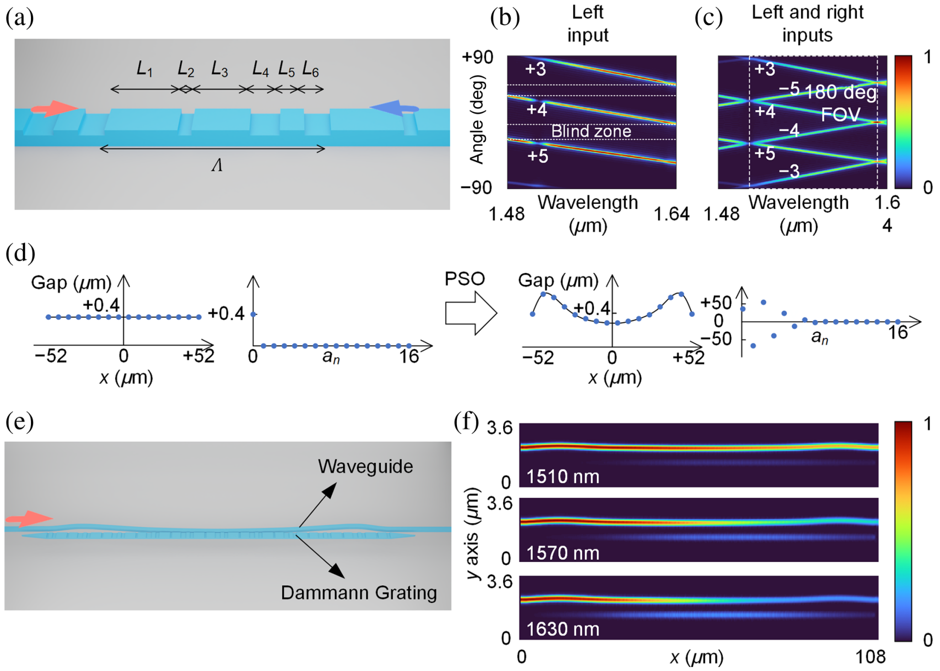

Fig. 2 (a) Schematic of the designed 1×3 Dammann grating. The grating pitch (Λ) is 2.6 μm, and the lengths of the various segments within the grating are $L_1 = 0.838\ \mu$m, $L_2 = 0.160\ \mu$m, $L_3 = 0.666\ \mu$m, $L_4 = 0.349\ \mu$m, $L_5 = 0.282\ \mu$m, and $L_6 = 0.305\ \mu$m. (b) Emitted diffraction orders +3, +4, and +5 of far-field patterns with the left input as a function of wavelength. The red regions indicate the blind zone. (c) Far-field patterns with left and right inputs as a function of wavelength. The dashed box indicates that six diffractions (orders ±3 through ±5) with bidirectional inputs cover a 180-deg FOV in the wavelength range of 1510 to 1630 nm. (d) Spacing between the waveguide and grating as a function of distance before and after PSO. (e) Schematic of the WG-DC structure. (f) Optical power distributions within the proposed WG-DC structure at 1510, 1570, and 1630 nm. The power distributions at these wavelengths resemble Gaussian distributions.

enlargement of the grating aperture and concurrently boosts the mode purities of OAM (Laguerre–Gaussian mode) beams. Because the waveguide is symmetric along the x axis, the spacing between the grating and the waveguide is a real, even function whose Fourier series is also a real, even function. The spacing between the grating and the waveguide is then apodized as a set of cosine series, $\sum a_n \cos(nx)$, as shown in Fig. 2(d). Neglecting the bend loss, the coefficients a_n are optimized using the particle swarm optimization (PSO) algorithm in MATLAB to achieve a Gaussian distribution in the power intensity (detailed in Supplementary Material S2).

The power in the strip waveguide and Dammann grating can be expressed as

$$\frac{\mathrm{d}P_w}{\mathrm{d}z} = -j\kappa_{wg}P_g e^{j2\delta z}, \frac{\mathrm{d}P_g}{\mathrm{d}z} = -j\kappa_{gw}P_w e^{-j2\delta z-\alpha z}, \tag{2}$$

where P_w and P_g are the complex amplitudes of the waveguide and grating, respectively; κ_{wg} and κ_{gw} are conjugated mode-coupling coefficients, which describe the interaction between the waveguide and the grating; and δ is the propagation constant of the guided mode, which equals that in the Dammann grating owing to the phase-matching condition. The loss factor α can be obtained from the 3D finite-difference time-domain (FDTD) simulation of the Dammann grating (see Supplementary Material S3 for the fitting of the loss factor of a grating and further discussion).

We define the figure of merit (FoM) to evaluate the similarity between the power distribution in the grating and the Gaussian distribution

$$\mathrm{FoM} = 1 - \mathrm{XCorr}[P_B, N(\mu, \sigma^2)], \tag{3}$$

where $N(\mu, \sigma^2)$ represents the Gaussian distribution characterized by the parameters $\mu = L_{\mathrm{grating}}/2$ and $\sigma^2 = L^2_{\mathrm{grating}}/16$, and XCorr represents the normalized cross-correlation of P_B and $N(\mu, \sigma^2)$ with a unity peak. We repeated the PSO algorithm 10 times, each with 200 iterations. All iterations converged to identical structural parameters, as shown in Fig. 2(d). The power distributions of the WG-DC at 1510, 1570, and 1630 nm are shown in Fig. 2(f).

3 Simulation and Experimental Demonstration

To validate and improve the performance of the proposed OAM OPA, we simulated a quasi-square OPA with dimensions of 104.0 μm × 106.4 μm. The simulated far-field intensities, amplitudes, and phase profiles, illustrated in Fig. 3(a), demonstrate the efficient conversion of guided modes into OAM modes with topological charges of +3, +4, and +5, respectively. As the wavelength increases from 1480 to 1640 nm, vortices that carry +3, +4, and +5 topological charges sweep angles from −40 to −13.5 deg, −7 to +20 deg, and +30 to +77 deg, respectively, indicating that an FOV of 154 deg can be achieved by injecting light from two sides of the OPA. Furthermore, the divergence angles of the $\mathrm{OAM}_{\pm 3}$, $\mathrm{OAM}_{\pm 4}$, and $\mathrm{OAM}_{\pm 5}$ beams are ∼3, 4, and 5 deg, respectively.

We fabricated an OAM OPA chip on a commercial 220-nm-thick SOI platform. Figure 3(d) shows the zoomed-in and microscopic images of the fabricated silicon OAM OPA chip. A fork structure can be observed at the center of the grating array. The fabricated chip was packaged using edge coupling and wire bonding and connected to a 64-channel voltage source via three 40-pin FPC connectors on the printed circuit board (PCB). The host computer controlled the 64-channel voltage source using a general-purpose interface bus (GPIB) connector. The detailed device fabrication and packing processes are described in Sec. 6.

Figure 3(e) shows a schematic of the experimental setup used to characterize the fabricated OAM OPA chip. A tunable laser source (Keysight 81960A) illuminated the fabricated device from 1505 to 1630 nm. The laser output was split into two branches using a 50:50 coupler. In the top branch, we used a polarization controller (PC) and variable optical attenuator (VOA) to control the polarization state and power of the light. After edge coupling, the guided TE_0 mode was split into 64 copies using a six-stage 1 × 2 MMI tree, and 56 copies were sent to the waveguide array. These TE_0 lights in the waveguide array were coupled to the 1 × 3 Dammann grating array (superposed holographic fork gratings) and emitted into free space as single-polarization OAM modes ($\mathrm{OAM}_{+3} - \mathrm{OAM}_{+5}$). The other branch served as a reference Gaussian beam, whose power and polarization were adjusted using a PC and a VOA. The generated OAM modes and reference Gaussian beams with the same polarization, proper relative powers, and spot sizes were combined using a beam splitter (BS) to obtain the interferogram. We used an infrared charge-coupled device (IR-CCD, Luster) to monitor the intensity profiles of the generated OAM modes and corresponding interferograms.

The phase mismatch of the input lights caused random intensity profiles of the OAM beams. We used a genetic algorithm (GA) to align the input phases of the OPA according to R^2, which is the coefficient of determination for fitting the intensity profiles to the ideal OAM intensity in MATLAB. Here, we take the generation of OAM_{+4} at 1565 nm as an example. As shown in the inset of Fig. 3(e), the measured intensity profile exhibits a donut shape owing to the phase singularity after 100 iterations of GA optimization (see Supplementary Material S3). We recorded the intensity profiles of the $\mathrm{OAM}_{+3} - \mathrm{OAM}_{+5}$ beams, as depicted in Fig. 3(b). These profiles closely match the corresponding far-field patterns shown in Fig. 3(a), demonstrating the effectiveness of the GA in aligning the phase profiles. The topological charges of the generated OAM beams can be confirmed by counting the number of twists and twist directions of the interferograms. To verify the polarization state of light, we removed the reference light and inserted a polarizer before the IR-CCD [not shown in Fig. 3(e)]. Figure 3(c) presents the intensity profiles with the polarizer axis rotated to 0 (horizontal), 45, and 90 deg (vertical), where the power of the generated y-polarized OAM_{+4} is gradually enhanced. A discussion of the GA used to control the voltages of the thermal phase shifters to reconstruct the OAM light is provided in the Supplementary Material.

4 Sweeping in θ and φ Directions

We measured the emission angles of the OAM beams to obtain the FOV along the θ axis of the fabricated device. Figure 4(b) presents the intensities measured at different wavelengths. The intensities of the far fields initially increase and then decrease with increasing wavelength, in contrast to the behavior of the simulated far-field shown in Fig. 4(a). This variation is due to the center wavelength of the 1 × 2 MMI, which is ∼1570 nm. Figure 4(c) illustrates emission angles of −39.47 to −13.68 deg,

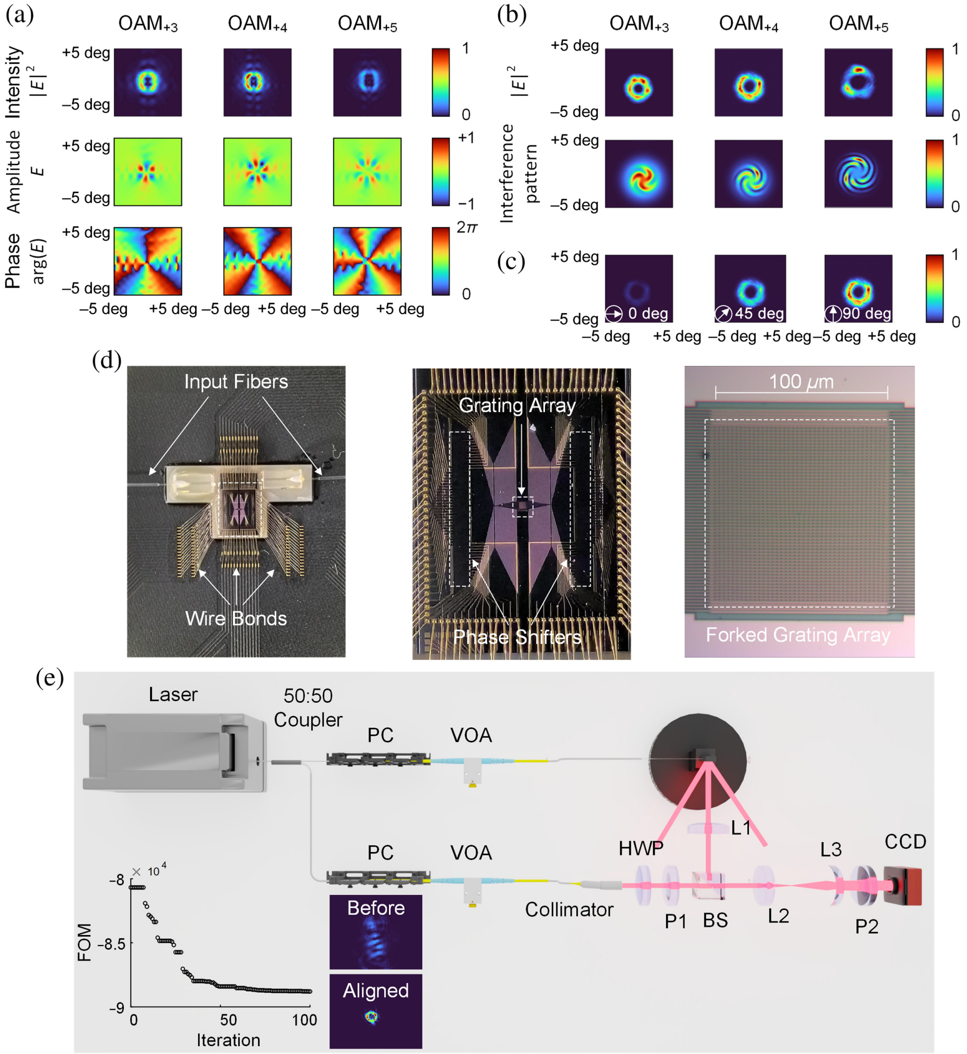

Fig. 3 Simulated and measured far-field intensities for vertical emission ($\varphi = 0$ deg). (a) Simulated far-field patterns, amplitudes, and phase profiles of three orders (+3, +4, and +5) at 1565 nm with left input. (b) Measured far-field intensities and interference patterns of the emitted OAM lights. (c) Measured far-field intensity profiles of the y-polarized OAM$_{+4}$ at 1565 nm following a rotation of the polarizer (0, 45, and 90 deg). The arrows indicate the angles of the polarizer. (d) Zoomed-in and microscopic images of the packaged device, consisting of the 3.5 mm × 4.5 mm multiple OAM OPA chip wire bonded to a silicon interposer, along with left and right optical fiber inputs. (e) Experimental setup used to characterize the far-field profiles of the multibeam OPA (laser: Keysight 81960A). PC, polarization controller; VOA, variable optical attenuator; HWP, half-wave plate; P1 and P2, polarizers; BS, beam splitter; L1, L2, and L3, lenses; IR-CCD, infrared charge-coupled device. Inset: FoM versus iteration and far-field profiles before and after phase alignment.

−6.60 to +20.52 deg, and +30.03 to +76.65 deg for OAM$_{+3}$, OAM$_{+4}$, and OAM$_{+5}$ beams, respectively, for a 1480- to 1640-nm input with left input. Specifically, within the wavelength range of 1505 to 1625 nm, the diffracted beams of the OAM OPA with bidirectional inputs covered an FOV of approximately −75 to +75 deg, as shown in the bottom images in Figs. 4(a) and 4(b). The FOV coverage and wavelength range in Fig. 4(c) agree well with the simulation results for the 1 × 3 Dammann grating.

In the φ direction, the maximum deflection angle of the 0'th-order far field, quantified as $\Delta\varphi = \pm[90\text{ deg} - \cos^{-1}(\lambda_{\min}/2\Lambda_y)]$, was approximately ±23.33 deg (Λ_y represents the period of the OPA in the y direction). If the phase differences among the neighboring waveguides are close to 180 deg, the far field will experience attenuation and distortion significantly; therefore, we limited the deflection angle of the chip to values from −20 to +20 deg. We adjusted the tilt angle of the OPA chip by −20, −10, 0, +10, and +20 deg with respect to the φ axis and repeated the fitting and optimization processes for 13 wavelengths in the range of 1505 to 1625 nm. The far-field profiles for the OAM$_{\pm 3}$ − OAM$_{\pm 5}$ beams with the left and right input, illustrated in Fig. 4(d), indicate the beam deflection of

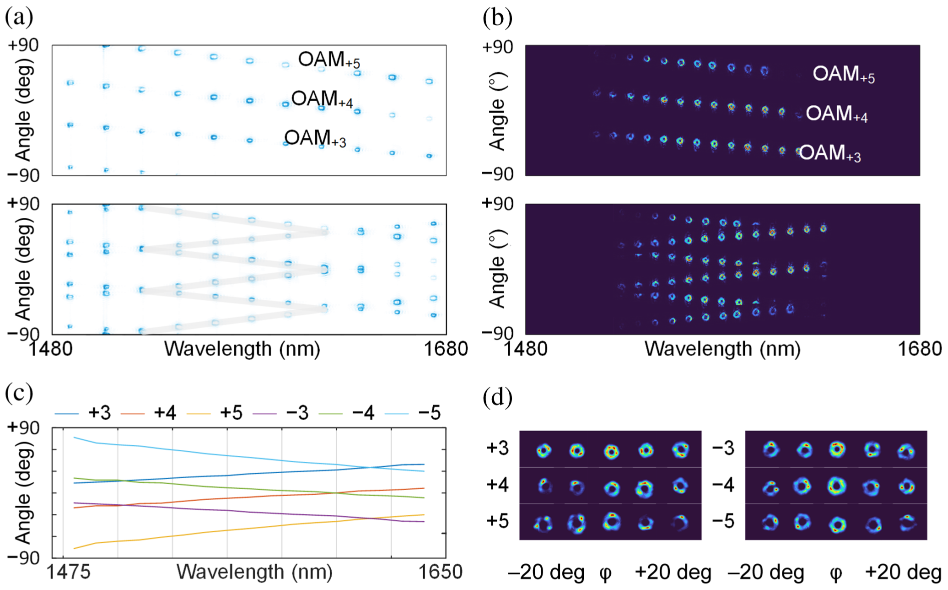

Fig. 4 Simulated and measured far-field intensities of emitted multiple vortices with different wavelength inputs. (a) and (b) Simulated and measured far-field emission patterns in a wavelength range from 1480 to 1640 nm with left input (up) and left and right inputs (down), respectively. (c) Angle sweeping of emitted diffraction orders ±3, ±4, and ±5 with bidirectional inputs. (d) Measured far fields of multiple vortices at different emission angles with respect to the φ axis.

multiple OAM beams. Using a tunable laser and thermal phase shifters to steer the light beams, the angular resolution is determined by the divergence angle of the OAM beam. The theoretical resolution is 31×9; however, for convenience and time efficiency, we used a 13×5 resolution in our experiments. Details of the far-field patterns are provided in the Supplementary Material.

5 Discussion

The experimental demonstration of a wide FOV, multibeam OPA marks a significant advancement in multibeam emission technology. This system uses different topological charges for precise beam steering. The direction of OAM beams with positive and negative topological charges can be controlled by adjusting the left and right thermal phase shifter arrays, respectively. Another key feature of our approach is the use of waveguide–grating directional couplers, which substantially increase the antenna aperture of the silicon grating compared with those of the conventional structures. Theoretically, three OPA chips can provide a complete 360-deg FOV, significantly reducing the number of optical components.

Our multibeam strategy accelerates angular scanning and maintains a wide FOV, enabling the use of fewer OPA chips in high-speed applications. Moreover, the proposed design is scalable; optimization of the grating size and reduction in the far-field spot diameter enhance adaptability. Including a nonredundant OPA using a Costas array can further expand the footprint of the aperture.[9] This scalability, along with the simplicity of the proposed WG-DC structure, makes the wide FOV, multi-OAM OPA a versatile and promising solution for high-precision optical beam steering in broadcast systems,[65–69] secure quantum communications,[55,70–74] applications in environments with complex atmospheric turbulence,[45,75] and detection of flying vehicle propellers.[76,77]

6 Appendix: Methods

Detailed descriptions of the optical simulation and optimization, characterization of the far field, and phase modulation of the thermal phase shifter are presented in the Supplementary Material.

6.1 Numerical Simulations

The numerical results presented in Figs. 2–4 were obtained through 3D FDTD simulations using the commercial software ANSYS Lumerical. In the simulation setup, the 3-μm-thick substrate layer and the 2-μm-thick cladding layer were SiO_2 with a refractive index of 1.44, and the material of the sandwiched waveguide was silicon with a refractive index of 3.47. The simulation region implemented a perfectly matched layer as the boundary condition, and a mesh accuracy of 2 was specified. Fifty-six mode sources were set to the fundamental transverse electric (TE_0) mode, and a frequency domain power monitor was positioned 1 μm above the interface between the cladding and air to capture the outgoing field.

6.2 Device Fabrication and Packaging

Based on the structure design, theory, and simulation results, the devices were fabricated on an SOI platform with a 220-nm-thick silicon top layer and a 3-μm-thick SiO_2 buried oxide layer. The waveguides and the Dammann grating array were patterned via electron beam lithography (Vistec EBPG-5200$^+$). Full and partial etching was performed using an inductively coupled plasma (ICP, SPTS) etching process. After that, a 2-μm-thick SiO_2 cladding layer was uniformly deposited on top of the devices using plasma-enhanced chemical vapor deposition (Oxford). A 400-nm-thick Ti layer functioned as a thermal phase shifter, and a 300-nm-thick gold layer was deposited using an e-beam evaporator (Denton Electron Beam Evaporator). Each phase shifter had a resistance of ∼5 kΩ. A total of 112 gold wires were bonded from the gold pads on the silicon chip to a PCB using F&S BONDTEC 53XXBDA.

6.3 Optical Performance Characterization Setup

To characterize the optical performance of the fabricated device, we used a continuous-wave tunable semiconductor laser source (Santec TSL-770) to generate light ranging from 1480 to 1640 nm. A 50:50 coupler was utilized to split the light into two beams, which were sent to two PCs. One of the beams was coupled to the fabricated chip, and the other was collimated using a collimator. The diffracted light and collimated beam were subsequently combined using a BS and captured using an IR-CCD equipped with a four-lens system.

Disclosures

The authors declare no competing interests.

Code and Data Availability

Data underlying the results presented in this paper may be obtained from the authors upon reasonable request.

Acknowledgements

This work was supported by the National Natural Science Foundation of China (Grant Nos. 62341508 and 62105203) and the Shanghai Municipal Science and Technology Major Project (Grant No. BH0300071). The authors thank the Center for Advanced Electronic Materials and Devices of Shanghai Jiao Tong University for its support in device fabrication.

References

1. R. Collis, "LiDAR," *Appl. Opt.* **9**(8), 1782–1788 (1970).
2. U. Wandinger, M. McCormick, and C. Weitkamp, *LiDAR: Range-Resolved Optical Remote Sensing of the Atmosphere*, Springer Series in Optical Sciences, C. Weitkamp, Ed., Vol. 102, pp. 1–18, Springer Berlin/Heidelberg (2005).
3. O. Wolf et al., "Phased-array sources based on nonlinear metamaterial nanocavities," *Nat. Commun.* **6**(1), 7667 (2015).
4. P. Hyde et al., "Exploring LiDAR–radar synergy—predicting aboveground biomass in a southwestern ponderosa pine forest using LiDAR, SAR and InSAR," *Remote Sens. Environ.* **106**(1), 28–38 (2007).
5. T. Raj et al., "A survey on lidar scanning mechanisms," *Electronics* **9**(5), 741 (2020).
6. P. Dong and Q. Chen, *LiDAR Remote Sensing and Applications*, CRC Press (2017).
7. J. K. Doylend et al., "Two-dimensional free-space beam steering with an optical phased array on silicon-on-insulator," *Opt. Express* **19**(22), 21595–21604 (2011).
8. J. Sun et al., "Large-scale nanophotonic phased array," *Nature* **493**(7431), 195–199 (2013).
9. T. Fukui et al., "Non-redundant optical phased array," *Optica* **8**(10), 1350–1358 (2021).
10. S. A. Miller et al., "Large-scale optical phased array using a low-power multi-pass silicon photonic platform," *Optica* **7**(1), 3–6 (2020).
11. P. Lu et al., "Integrated multi-beam optical phased array based on a 4 × 4 Butler matrix," *Opt. Lett.* **46**(7), 1566–1569 (2021).
12. D. Kwong et al., "On-chip silicon optical phased array for two-dimensional beam steering," *Opt. Lett.* **39**(4), 941–944 (2014).
13. K. Van Acoleyen et al., "Off-chip beam steering with a one-dimensional optical phased array on silicon-on-insulator," *Opt. Lett.* **34**(9), 1477–1479 (2009).
14. D. J. Lum, "Ultrafast time-of-flight 3D LiDAR," *Nat. Photonics* **14**(1), 2–4 (2020).
15. Y. Jiang, S. Karpf, and B. Jalali, "Time-stretch LiDAR as a spectrally scanned time-of-flight ranging camera," *Nat. Photonics* **14**(1), 14–18 (2020).
16. T. Inomata et al., "Origins and spread of formal ceremonial complexes in the Olmec and Maya regions revealed by airborne LiDAR," *Nat. Hum. Behav.* **5**(11), 1487–1501 (2021).
17. M. Brydegaard et al., "LiDAR reveals activity anomaly of malaria vectors during pan-African eclipse," *Sci. Adv.* **6**(20), eaay5487 (2020).
18. J. Tachella et al., "Real-time 3D reconstruction from single-photon LiDAR data using plug-and-play point cloud denoisers," *Nat. Commun.* **10**(1), 4984 (2019).
19. J. Park et al., "All-solid-state spatial light modulator with independent phase and amplitude control for three-dimensional LiDAR applications," *Nat. Nanotechnol.* **16**(1), 69–76 (2021).
20. R. Tobin et al., "Robust real-time 3D imaging of moving scenes through atmospheric obscurant using single-photon LiDAR," *Sci. Rep.* **11**(1), 11236 (2021).
21. C.-P. Hsu et al., "A review and perspective on optical phased array for automotive LiDAR," *IEEE J. Sel. Top. Quantum Electron.* **27**(1), 1–16 (2020).
22. C. V. Poulton et al., "Long-range LiDAR and free-space data communication with high-performance optical phased arrays," *IEEE J. Sel. Top. Quantum Electron.* **25**(5), 1–8 (2019).
23. W. S. Rabinovich et al., "Free space optical communication link using a silicon photonic optical phased array," *Proc. SPIE* **9354**, 93540B (2015).
24. S. Royo and M. Ballesta-Garcia, "An overview of LiDAR imaging systems for autonomous vehicles," *Appl. Sci.* **9**(19), 4093 (2019).
25. J. Choi et al., "Multi-target tracking using a 3D-LiDAR sensor for autonomous vehicles," in *16th Int. IEEE Conf. Intell. Transp. Syst. (ITSC 2013)*, pp. 881–886 (2013).
26. Y. Guo et al., "Integrated optical phased arrays for beam forming and steering," *Appl. Sci.* **11**(9), 4017 (2021).
27. Y. Liu et al., "A single-chip multi-beam steering optical phased array: design rules and simulations," *Opt. Express* **29**(5), 7049–7059 (2021).
28. Y. Liu et al., "On-chip multi-beam emitting optical phased array for wide-angle LiDAR," in *CLEO: Appl. and Technol.*, p. JTu2G.25 (2020).
29. C. Liu et al., "High-resolution 3D imaging with a low-pixel APD array through multi-beam scanning of fiber-type OPA," in *Sixteenth Natl. Conf. Laser Technol. and Optoelectron.*, pp. 750–754 (2021).
30. Y. Wu et al., "Multi-beam optical phase array for long-range LiDAR and free-space data communication," *Opt. Laser Technol.* **151**, 108027 (2022).
31. G. He et al., "A review of multibeam phased array antennas as LEO satellite constellation ground station," *IEEE Access* **9**, 147142–147154 (2021).
32. A. Jacomb-Hood and E. Lier, "Multibeam active phased arrays for communications satellites," *IEEE Microwave Mag.* **1**(4), 40–47 (2000).
33. G. Toso, P. Angeletti, and C. Mangenot, "Multibeam antennas based on phased arrays: an overview on recent ESA developments," in *8th Eur. Conf. Antennas and Propag. (EuCAP 2014)*, pp. 178–181 (2014).
34. S. Prasad et al., "mmWave multibeam phased array antenna for 5G applications," *J. Electromagn. Wave* **35**(13), 1802–1814 (2021).
35. Z. Zhou et al., "Butler matrix enabled multi-beam optical phased array for two-dimensional beam-steering," in *27th OptoElectron. and Commun. Conf. (OECC) and Int. Conf. Photonics in Switch. and Comput. (PSC)*, pp. 1–3 (2022).

36. Y. Wu, S. Shao, and D. Che, "Fast and low grating lobe multibeam steering with a subarray level unequally spaced optical phased array," *JOSA B* **38**(11), 3417–3424 (2021).
37. K. Yoneda et al., "Vehicle localization using 76 GHz omnidirectional millimeter-wave radar for winter automated driving," in *IEEE Intell. Veh. Symp. (IV)*, pp. 971–977 (2018).
38. J. De Wit, W. Van Rossum, and A. De Jong, "Orthogonal waveforms for FMCW MIMO radar," in *IEEE RadarCon (RADAR)* (2011).
39. G. Chang et al., "Orthogonal waveform with multiple diversities for MIMO radar," *IEEE Sens. J.* **18**(11), 4462–4476 (2018).
40. D. Wu et al., "Multi-beam single-photon LiDAR with hybrid multiplexing in wavelength and time," *Opt. Laser Technol.* **145**, 107477 (2022).
41. C. Weimer et al., "LiDARs utilizing vortex laser beams," *Proc. SPIE* **10631**, 106310Q (2018).
42. N. Bozinovic et al., "Terabit-scale orbital angular momentum mode division multiplexing in fibers," *Science* **340**(6140), 1545–1548 (2013).
43. J. Wang et al., *Optical Fiber Telecommunications VIB: Chapter 12. Multimode Communications Using Orbital Angular Momentum*, Academic Press (2013).
44. J. Wang et al., "Terabit free-space data transmission employing orbital angular momentum multiplexing," *Nat. Photonics* **6**(7), 488–496 (2012).
45. Y. Shen et al., "Optical vortices 30 years on: OAM manipulation from topological charge to multiple singularities," *Light: Sci. Appl.* **8**(1), 90 (2019).
46. S. Zhang et al., "Broadband detection of multiple spin and orbital angular momenta via dielectric metasurface," *Laser Photonics Rev.* **14**(9), 2000062 (2020).
47. D. R. Gozzard et al., "Optical vortex beams with controllable orbital angular momentum using an optical phased array," *OSA Contin.* **3**(12), 3399–3406 (2020).
48. Y. Weng and Z. Pan, "Orbital angular momentum based sensing and their applications: a review," *J. Lightwave Technol.* **41**(7), 2007–2016 (2022).
49. B. Cochenour et al., "The detection of objects in a turbid underwater medium using orbital angular momentum (OAM)," *Proc. SPIE* **10186**, 1018603 (2017).
50. N. Dostart et al., "Serpentine optical phased arrays for scalable integrated photonic LiDAR beam steering," *Optica* **7**(6), 726–733 (2020).
51. K. Sayyah et al., "Two-dimensional pseudo-random optical phased array based on tandem optical injection locking of vertical cavity surface emitting lasers," *Opt. Express* **23**(15), 19405–19416 (2015).
52. S. Chung, H. Abediasl, and H. Hashemi, "A monolithically integrated large-scale optical phased array in silicon-on-insulator CMOS," *IEEE J. Solid-State Circuits* **53**(1), 275–296 (2017).
53. K. Van Acoleyen, H. Rogier, and R. Baets, "Two-dimensional optical phased array antenna on silicon-on-insulator," *Opt. Express* **18**(13), 13655–13660 (2010).
54. O. A. Saraereh, "Design and performance evaluation of OAM-antennas: a comparative review," *IEEE Access* **11**, 27992–28013 (2023).
55. R. Chen et al., "Orbital angular momentum waves: generation, detection, and emerging applications," *IEEE Commun. Surv. Tutor.* **22**(2), 840–868 (2019).
56. K. Liu et al., "Microwave-sensing technology using orbital angular momentum: overview of its advantages," *IEEE Veh. Technol. Mag.* **14**(2), 112–118 (2019).
57. K. Liu et al., "Orbital-angular-momentum-based electromagnetic vortex imaging," *IEEE Antennas Wireless Propag. Lett.* **14**, 711–714 (2014).
58. K. Liu et al., "Generation of OAM beams using phased array in the microwave band," *IEEE Trans. Antennas Propag.* **64**(9), 3850–3857 (2016).
59. J. Long et al., "High-power mode-programmable orbital angular momentum beam emitter with an internally sensed optical phased array," *Chin. Opt. Lett.* **22**(2), 021402 (2024).
60. K. Yang et al., "Modulating and identifying an arbitrary curvilinear phased optical vortex array of high-order orbital angular momentum," *Opt. Laser Technol.* **168**, 109984 (2024).
61. Y. Chen et al., "Integrated phased array for scalable vortex beam multiplexing," *J. Lightwave Technol.* **41**(7), 2070–2078 (2022).
62. R. M. Fouda et al., "Experimental BER performance of quasicircular array antenna for OAM communications," *IEEE Antennas Wireless Propag. Lett.* **19**(8), 1350–1354 (2020).
63. P.-Y. Feng, S.-W. Qu, and S. Yang, "OAM-generating transmitarray antenna with circular phased array antenna feed," *IEEE Trans. Antennas Propag.* **68**(6), 4540–4548 (2020).
64. N. Zhou et al., "Ultra-compact broadband polarization diversity orbital angular momentum generator with $3.6 \times 3.6\ \mu\text{m}^2$ footprint," *Sci. Adv.* **5**(5), eaau9593 (2019).
65. P. Hall and S. Vetterlein, "Review of radio frequency beamforming techniques for scanned and multiple beam antennas," in *IEE Proc. H (Microwaves, Antennas and Propag.)*, pp. 293–303 (1990).
66. Y. Aslan et al., "Orthogonal versus zero-forced beamforming in multibeam antenna systems: review and challenges for future wireless networks," *IEEE Journal of Microwaves* **1**(4), 879–901 (2021).
67. H. Wolf et al., "Satellite multibeam antennas at airbus defence and space: state of the art and trends," in *8th Eur. Conf. Antennas and Propag. (EuCAP 2014)*, pp. 182–185 (2014).
68. D. Striccoli, G. Piro, and G. Boggia, "Multicast and broadcast services over mobile networks: a survey on standardized approaches and scientific outcomes," *IEEE Commun. Surv. Tutor.* **21**(2), 1020–1063 (2018).
69. N. Chukhno et al., "Models, methods, and solutions for multicasting in 5G/6G mmwave and sub-THz systems," *IEEE Commun. Surv. Tutor.* **26**(1), 119–159 (2023).
70. I. B. Djordjevic, "Multidimensional OAM-based secure high-speed wireless communications," *IEEE Access* **5**, 16416–16428 (2017).
71. M. Zhang et al., "Physical layer key generation for secure OAM communication systems," *IEEE Trans. Veh. Technol.* **71**(11), 12397–12401 (2022).
72. M. A. B. Abbasi et al., "Physical layer secure communication using orbital angular momentum transmitter and a single-antenna receiver," *IEEE Trans. Antennas Propag.* **68**(7), 5583–5591 (2020).
73. J. Wang et al., "Orbital angular momentum and beyond in free-space optical communications," *Nanophotonics* **11**(4), 645–680 (2022).
74. A. E. Willner et al., "Optical communications using orbital angular momentum beams," *Adv. Opt. Photonics* **7**(1), 66–106 (2015).
75. S. Li et al., "Atmospheric turbulence compensation in orbital angular momentum communications: advances and perspectives," *Opt. Commun.* **408**, 68–81 (2018).
76. L. Marrucci, "Spinning the Doppler effect," *Science* **341**(6145), 464–465 (2013).
77. M. P. Lavery et al., "Detection of a spinning object using light's orbital angular momentum," *Science* **341**(6145), 537–540 (2013).

Zhen Wang received his PhD from the Department of Electronic Engineering, Shanghai Jiao Tong University, Shanghai, China, in 2024. He is currently a postdoctoral fellow at the Shanghai Institute of Optics and Fine Mechanics, Chinese Academy of Sciences, Shanghai, China. His current research interests include silicon photonics, optical phased arrays, and mode multiplexing technologies.

Yikai Su received his PhD in electrical engineering from Northwestern University, Evanston, Illinois, United States, in 2001. He served at Crawford Hill Laboratory of Bell Laboratories and joined Shanghai Jiao Tong University, Shanghai, China, as a full professor in 2004. His research areas cover silicon photonic devices, optical transmission, and signal processing. He has published over 600 publications and has given >70 invited talks at conferences including OFC, CLEO, and IPS. He is a senior member of IEEE and a fellow of Optica.

Biographies of the other authors are not available.